JME

Journal of Mining & Environment,
Vol.4, No.2, 2013, 83-96.

Adaptive neuro-fuzzy inference system application for hydrothermal alteration mapping using ASTER data

S. Mojedifar[1*], H. Ranjbar[1], H. Nezamabadi-pour[2]

1. Department of Mining Engineering, Shahid Bahonar University of Kerman,Iran
2. Department of Electrical Engineering, Shahid Bahonar University of Kerman, Iran

Received 21 October 2012; received in revised form 12 April 2013; accepted 15 September 2013
**Corresponding author: saeid_miner64@yahoo.com (S. Mojedifar).*

Abstract
The main problem associated with the traditional approach to image classification for the mapping of hydrothermal alteration is that materials not associated with hydrothermal alteration may be erroneously classified as hydrothermally altered due to the similar spectral properties of altered and unaltered minerals. The major objective of this paper is to investigate the potential of a neuro-fuzzy system in overcoming this problem. The proposed system is applied to the north western part of the Kerman Cenozoic Magmatic Arc, which hosts many areas of porphyry and vein-type copper mineralization. A software program based on an Adaptive Neuro-Fuzzy Inference System (ANFIS) was developed using the MATLAB ANFIS toolbox. The ANFIS program was used to classify Advanced Space-borne Thermal Emission and Reflection Radiometer, data based on the spectral properties of altered and unaltered rocks. The ANFIS result was then compared with other classified images based on artificial neural networks (ANN) and the maximum likelihood classifier (MLC). The verification of the results, based on field and laboratory investigations, revealed that the ANFIS method produces a more accurate map of the distribution of alteration than that obtained using ANN or MLC.

Keywords: *Mineral exploration, Remote sensing, Image classification, ANFIS, Hydrothermal alteration.*

1. Introduction

Geological remote sensing research has focused on the use of spectral signatures for the discrimination of different rock types, and the mapping of structures and the distribution of various minerals, especially hydrothermally altered minerals associated with mineralization. The launching of the Advanced Spaceborne Thermal Emission and Reflection Radiometer (ASTER) sensor has provided geologists with multispectral sensors in a space that provide data for the mapping of hydrothermal minerals and for lithological mapping. The visible-near infrared (VNIR) and shortwave infrared (SWIR) bands of ASTER are shown in Figure 1. For details on the characteristics of ASTER's sensor, see Yamaguchi et al. [2]. The ASTER sensor has been shown to achieve a high degree of accuracy in the spectral identification of rocks and minerals [3, 4]. Various methods for regional mapping of phyllic and argillic alteration using ASTER data were developed. Hydroxyl-bearing minerals are the most widespread products of hydrothermal alteration. Clays and sheet silicates, which contain Al-OH- and Mg-OH-bearing minerals and hydroxides in alteration zones, are characterized by absorption bands in the 2.1–2.4 μm range due to molecular vibrational processes (Figure 1). High concentrations of clays and sheet silicates are characterized by very high reflectance in band 4 of ASTER data. These characteristics of phyllosilicates have been used in remote sensing investigations for mineral exploration (e.g., [5, 6, 7, 8].The presence of water in vegetative tissue commonly results in spectral interference with hydroxyl-bearing minerals. As an additional complication, situations also arise in which

minerals such as clays are present in both hydrothermal systems and in unaltered sedimentary rocks. Discrimination between these two types of clay minerals is difficult when using standard image-processing techniques such as band rationing, principal component analysis, or spectral angle mapper. In other words, the mentioned methods are not useful in distinguishing alteration zones in unaltered and vegetation regions. In recent years, several attempts were made to extract altered regions in the areas covered with vegetation. Abrams et al. [9] mapped hydrothermal alteration using digitally processed aircraft multispectral images. Kaufmann [10] mapped hydrothermal alteration using digitally processed TM images. Knepper and Simpson [11] used TM color ratio composite images to recognize hydrothermally-altered rocks. Bennett et al. [12] integrated TM data with field and laboratory data to discover alteration zones. Goosens and Kroonenberg [13] used TM ratio images to identify rocks overlain by residual soil. Carranza and Hale [14] integrated results of TM images and ground data to map hydrothermal alteration. Porwal et al. [15] applied a neuro-fuzzy system in preparing a mineral potential map from several exploratory datasets. Honarmand et al. [16] used principal component analysis and spectral angle mapper to discover hydrothermal alteration minerals. Budradduza and Fujimitsu [17] tried to distinguish alteration zones using the colour composite, band ratio, principal component, least square fitting and reference spectra analysis. In recent studies, the use of Fuzzy Control and Fuzzy Set theory has rapidly expanded into remote sensing. Another soft computing technique that has received attention in many applications is artificial neural networks (ANN). ANN does not require a well-defined physical relationship to systematically map input vectors to target values (vectors); instead, all that is needed for most networks is a collection of representative examples (input–output pairs) of the desired mapping elements.

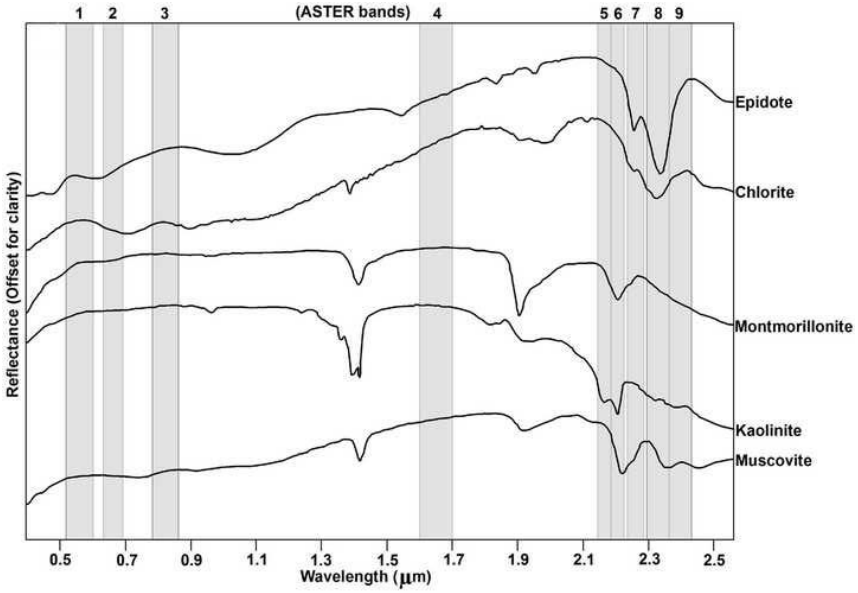

Figure 1. Reflectance spectra of common hydrothermal minerals The bands' widths of ASTER are shown in grey. The spectra are taken from [1].

The above techniques have proven to be effective when used individually; however, the integration of neural networks and fuzzy logic has given birth to neuro-fuzzy systems with the potential to capture the benefits of both of these approaches in a single framework. Neuro-fuzzy systems eliminate the basic problem encountered in fuzzy system design (i.e., obtaining a set of fuzzy if–then rules) by effectively using the learning capability of an ANN for automatic fuzzy if–then rule generation and parameter optimization [18].

The main objective of this paper is to investigate the potential of a neuro-fuzzy system in mapping the distribution of hydrothermally altered areas. The mapped areas are compared with the results obtained using other classification techniques; i.e., the maximum likelihood classifier, MLC, and ANN.

2. Data pre-processing

We used three ASTER scenes previously pre-processed up to Level 1B.Two scenes were acquired on 18 April 2000 and one scene was acquired on 15 June 2007. These scenes were georeferenced using an orthorectified enhanced thematic mapper plus (ETM+) image in the UTM projection (zone 40) with theWGS-84 ellipsoid as a datum. The first two scenes were corrected for Crosstalk. Internal Average Relative Reflectance (IARR) correction was also applied on the images. The data sets were then mosaicked (Figure 2).

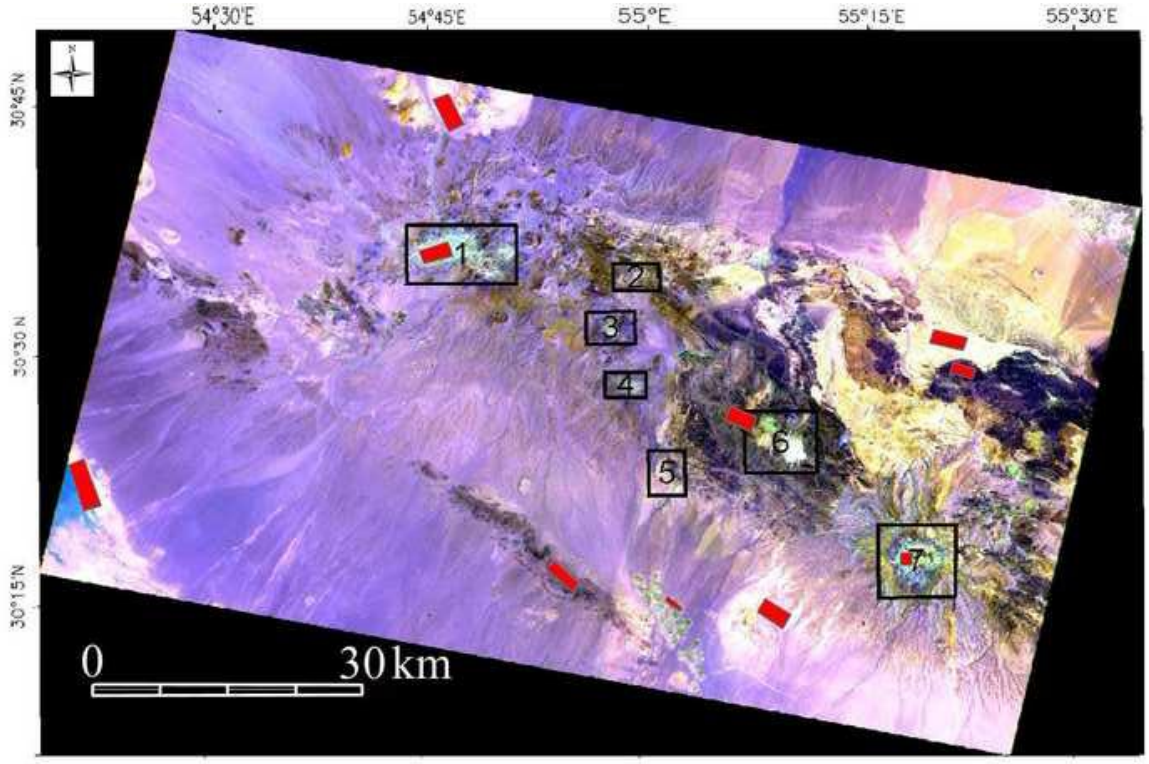

Figure 2. Colour composite of ASTER images (band 6 in red, band 4 in green and band 1 in blue). The vegetation cover is shown in green. The mineralized areas are outlined by boxes:1) Kader, 2) Godekolvari, 3) Iju, 4) Serenu, 5) Chahfiroozeh, 6) Meiduk and Parkam, and 7) Abdar. The red polygons indicate training areas for the classification methods.

3. Methodology

The neuro-fuzzy program was developed using the MATLAB ANFIS (Adaptive Neuro-Fuzzy Inference System) toolbox. ASTER images were also analysed by MLC and ANN in order to compare their results with the ANFIS classified image. For ground trothing, the altered areas mapped with these methods were examined in the field, and samples were collected for the preparation of thin sections and for X-ray diffraction analysis.

3.1. MLC and ANN

The objective of image classification procedures is to automatically categorize pixels in an image into land cover classes or themes [19]. The spectral pattern present within the data for each pixel is used as the numerical basis for classification. MLC quantitatively evaluates both the variance and covariance of the category spectral response patterns when classifying an unknown pixel. The probability density functions are used to classify an unidentified pixel by computing the probability of the pixel value belonging to each category. After evaluating the probability in each category, the pixel is assigned to the most likely class. It is assumed that the cloud of points forming the category training data has a normal distribution [19].

The ANN classifier is an information-processing model based on a simplification of our perception of how the neurons and synapses in the human brain process data. The model consists of a number of highly inter-connected processing elements that are analogous to neurons. These are connected by weighting junctions that are analogous to synapses. A typical two-layer NN has a first layer as input data, the intermediate or hidden layer as synopses, and a final layer that represents the output neurons. The sum of the products of the input values and the synapse

weights in the first hidden layers are transformed using a thresholding function into output values from the hidden layer. These output values of a hidden layer are then used as input values in a similar process for the second hidden layer. The results of the output of the last hidden layer in the ANN are sent to the output neurons. The ANN classifier has to train its synopses so that its output values match the actual class values. A set of training sites with known pixel data values and class assignment are used to train the ANN classifier by adjusting the weights until the output class assignment from the ANN matches the actual class value [20].

3.2. Adaptive neuro-fuzzy inference system (ANFIS)

ANFIS is a TSK fuzzy model placed in the framework of adaptive systems to facilitate learning and adaptation [18]. Such a framework makes the ANFIS modelling more systematic and less reliant on expert knowledge. An adaptive neuro-fuzzy system is an inference system in which a universal approximator is expressed to represent non-linear functions [21]. An adaptive neural network is a network structure consisting of a number of nodes connected through directional links. Each node is characterized by a node function with fixed or adjustable parameters. The learning or training phase of a neural network is employed to determine parameter values to fit the training data efficiently. Once the fuzzy inference system is initialized, neural network algorithms can be used to determine the unknown parameters (premise and consequent parameters of the rules), minimizing the error measured (e.g., the mean square error (MSE), which is the error between the desired output and system output) [22]. Reflecting the nature of this optimization procedure, the system is referred to as "adaptive". An example of an adaptive network is shown in Figure 3b, which is functionally equivalent to the fuzzy inference system shown in Figure 3a.

ANFIS, developed by Jang [18], consists of the following five layers.

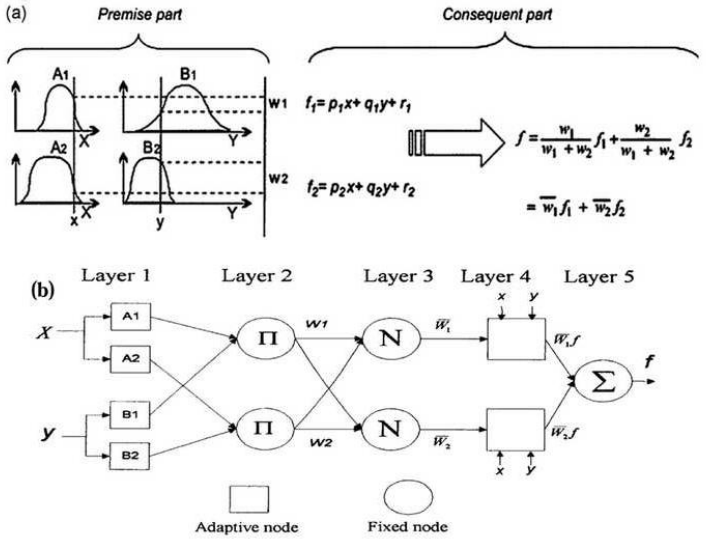

Figure 3. (a) Schematic architecture of the fuzzy model of ANFIS. (b) Schematic architecture of the network-based model of ANFIS (after Jang, [18]).

Layer 1: Each node in this layer generates a membership grade of a linguistic label. For instance, the node function of the i[th] node might be

$$O_i^1 = \mu_{A_i}(x) = \frac{1}{1+\left[\left(\frac{x-v_i}{\sigma_i}\right)^2\right]^{b_i}} \quad (1)$$

where, x is the input to node i, $\mathbf{O_i^1}$ is the output of the i[th] node in layer1, A_i is the linguistic label (small, large, etc.) associated with this node, and $\{\sigma_i, v_i, b_i\}$ is the parameter set that changes the shapes of the membership functions. Parameters in this layer are referred to as "premise parameters".

Layer 2: Each node in this layer calculates the "firing strength" [18] of each rule via multiplication:

$$O_i^2 = W_i = \mu_{A_i}(x).\mu_{B_i}(y) \quad (2)$$

where, O_i^2 is the output of the i[th] node in layer 2.

Layer 3: The i[th] node of layer 3 calculates the ratio of the i[th] rule's firing strength to the sum of all rules' firing strengths:

$$O_i^3 = \bar{W}_i = \frac{W_i}{\sum_{i=1}^{n} X_j} \qquad \text{i=1,2} \tag{3}$$

where, O_i^3 is the output of the i[th] node in layer 3 and W_i is the firing strength of the i[th] node in layer 3. For convenience, the outputs of this layer are referred to as "normalized firing" strengths.

Layer 4: Every node i in this layer is a node function:

$$O_i^4 = \bar{W}_i f_i = \bar{W}_i (p_i x + q_i y + r_i) \tag{4}$$

where, W_i is the output of layer 3, O_i^4 is the output of the i[th] node in layer 4 and f_i is the weighted linear combination of the crisp inputs. Parameters in this layer are referred to as "consequent parameters".

Layer 5: The single node in layer 5 is a circle node labelled "R" that computes the "overall output" as the summation of all incoming signals; i.e,

$$O_i^5 = Overall\ Output = \sum \bar{W}_i f_i = \frac{\sum W_i f_i}{\sum W_i} \tag{5}$$

The basic learning rule of ANFIS is back-propagation gradient descent [18], which calculates error signals (defined as the derivative of the squared error with respect to each node's output) from the output layer backward to the input nodes. To know more about ANFIS, It is recommended to refer to Jang [18].

4. Geology of the study area

The study area is part of the Central Iranian Cenozoic Magmatic Belt ,CICMB, which runs parallel to the Zagros geo-suture for about 1800 km from Azerbaijan Province of Iran in the northwest to north of Makran in the southeast (Figure 4).

The area is located in the Kerman Cenozoic magmatic arc, KCMA, which is part of the southeastern sector of the CICMB. The KCMA is 40–50 km wide and trends northwest–southeast for approximately 400 km along the southern margin of the central Iran micro-continent.

The oldest rocks in the study area are Cretaceous coloured mélange that consists of sedimentary and volcanic rocks. The youngest rocks are Quaternary alluvial deposits and gravel fans (Figure 4). Cretaceous sediments are mainly flysch. Eocene volcanic rocks are subdivided into the Bahr-e-Aseman complex and the Lower Razak, Middle Razak, and Upper Razak complexes. These rocks comprise pyroclastics, pyroxene trachyandesites, pyroxene andesites, trachyandesites, trachybasalts, tuffaceous sediments, basaltic rocks and andesites. The sedimentary rocks in the volcanic–sedimentary complex are mainly sandstone and minor limestone. The Eocene volcanic sedimentary rocks are intruded by Oligocene–Miocene plutons of granodiorite, quartz-diorite, diorite, monzonite, tonalite and granite. The volcanic rocks near these intrusives are widely metamorphosed and altered. Most of the plutonic and volcanic rocks are hydrothermally altered and locally mineralized. Argillic, sericitic and propylitic alteration are the most common types of hydrothermal alteration in the area. The Neogene sediments consist mainly of loosely consolidated, unsorted and poorly stratified conglomerate and sandstone overlying the Eocene volcanic–sedimentary rocks. Calcareous terraces and recent alluvium are the main Quaternary sediments. The Dehaj and Aj phases of volcanic activity, which produced pyroclastic, dacitic and basaltic rocks, occurred in the Pliocene [23]. The study area contains copper mineralization at Meiduk, Abdar, Kader, Godekolvari, Iju, Serenu, Chahfiroozeh and Parkam.

5. Data analysis and results

5.1. MLC and ANN

ASTER data were classified using MLC and NN methods, based on altered and unaltered classes. The training sites (see Figure 2) were chosen based on field and laboratory studies. Figures 5A and 5B show the classified results obtained using ANN and MLC, respectively.

5.2. ANFIS

A collection of well-distributed, sufficient and accurately measured input training data is a basic requirement in obtaining an accurate model. The selection of ANFIS inputs (variables) is the most important step in designing the model.

In the present application, there are two classes: presence or absence of alteration. VNIR and SWIR data (bands 1–9) of the ASTER instrument were used as inputs for the neuro-fuzzy system.

Training areas were selected for classification by ANFIS (Figure 2). The altered training area was chosen in known alteration zones (phyllic and argillic zones that contain sericite and clay minerals such as illite and montmorillonite).

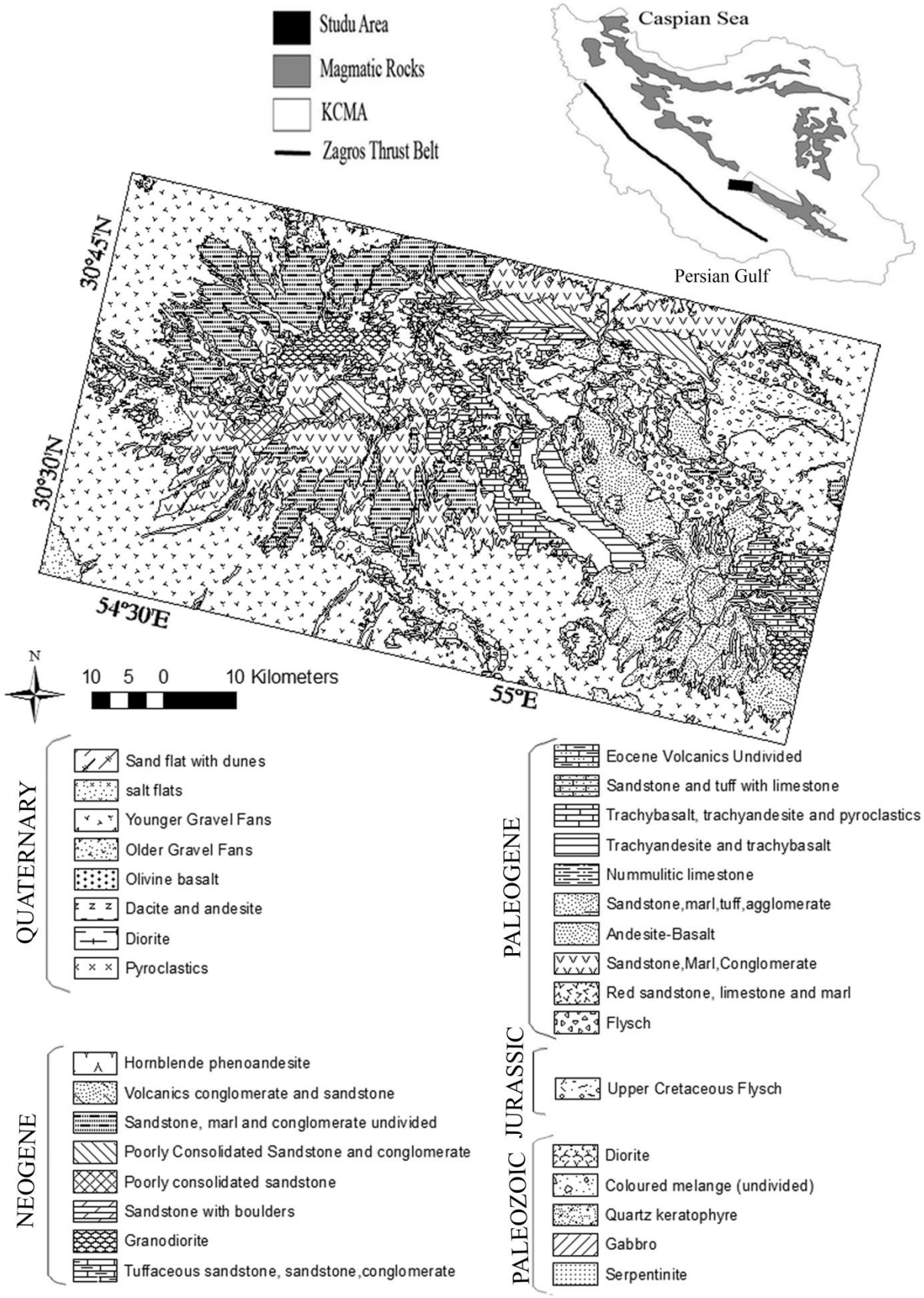

Figure 4. Geological map of the study area (modified after Soheili, [23]). A location map of the area is shown with respect to the location of the Kerman Cenozoic Magmatic Arc.

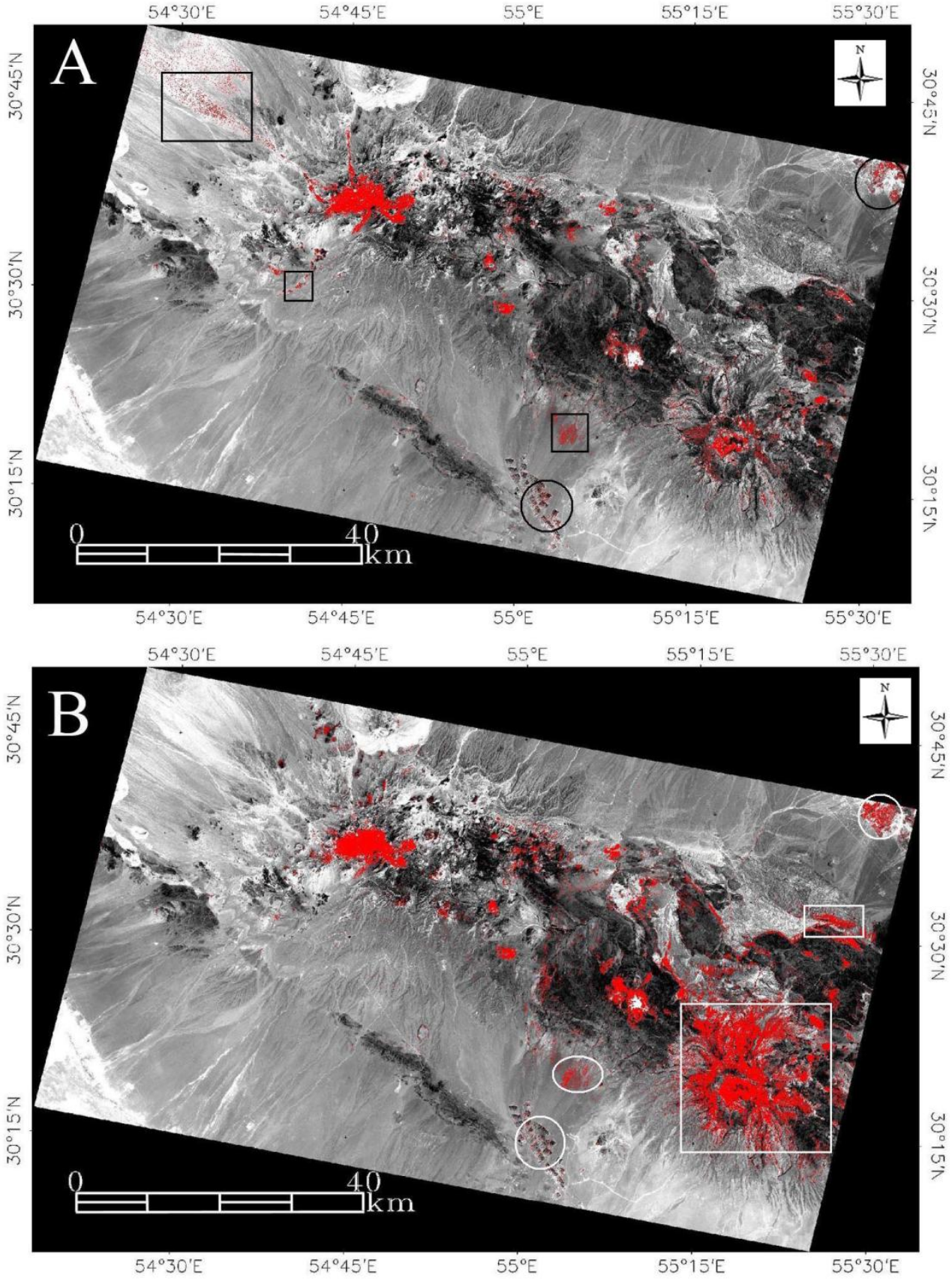

Figure 5. Results obtained by ANN classification (A) and by MLC classification (B). The classified areas are draped over band 1 of ASTER.

The unaltered training area includes the areas with vegetation cover (to eliminate vegetation spectral interference), unaltered areas of igneous rocks, and areas of sedimentary and carbonate rocks that contain clay minerals with similar spectral properties to those of altered areas. To achieve a good generalization capability of the ANFIS, it is important that the number of training datasets is larger than the number of modifiable parameters being estimated. Table 1 show the training and test pixels used in error evaluation as part of the training procedure.

Table 1. Confusion matrix of the testing and training data.

Testing Data		Predicted (ANFIS)	
		Alteration	non Alteration
Actual	Alteration	238	4
	non Alteration	8	1047
Training Data		Predicted (ANFIS)	
		Alteration	non Alteration
Actual	Alteration	883	63
	non Alteration	5	4215

5.2.1. ANFIS model for mapping the distribution of alteration

TSK FIS is implemented based on the subtractive clustering model (SCM) for mapping the distribution of alteration (Figure 6). Bands 1–9 of ASTER data were entered into the ANFIS model. The training datasets were used to verify the accuracy and effectiveness of each trained ANFIS model for the mapping of alteration. The proposed model was trained with 5166 pixels for the training phase. Figure 7 compares the final (post-training) Gaussian-shaped membership functions with the initial (before training) membership functions of the input parameters.

5.2.2. Accuracy assessment of ANFIS classification

After training, 1297 pixels employed as testing data were used to validate the accuracy of the ANFIS model for classification of the alteration area. Furthermore, in another set, the training data that were used to implement the ANFIS structure applied again to predict by ANFIS model and their results are presented in Table 1. The numbers of training pixels within altered and unaltered areas were 946 and 4220, respectively. To assess the performance of the ANFIS model, we used the Variance Account For (VAF) and the Root Mean Square Error (RMSE) [24] performance indices, were computed as follows:

$$VAF = \left(1 - \frac{\mathrm{var}(y - y')}{\mathrm{var}(y)}\right) \quad (6)$$

$$RMSE = \frac{1}{N}\sum_{i=1}^{n}(y - y')^2 \quad (7)$$

where, var denotes the variance; y and y' are the measured and predicted values, respectively; and N is the number of samples.

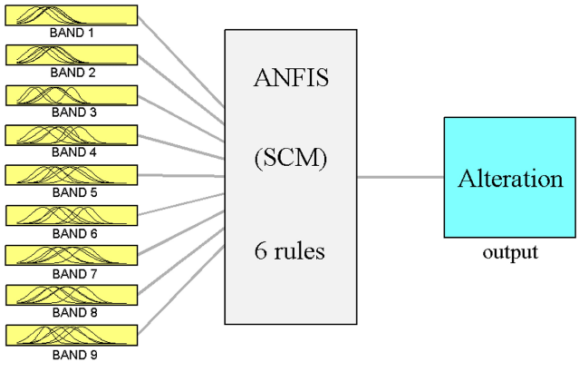

Figure 6. Schematic architecture of inputs and output for the ANFIS model.

The higher the VAF, the better is model performance. The RMSE and VAF indices were calculated to be 0.1126 and 91.47% for ANFIS, respectively. In addition, the classification results of the ANFIS model were displayed using a confusion matrix. The ANFIS model is represented by outputs restricted to within the range from 0 to 1, so they represent the probability of class membership. Note also that the optimal accuracy for the classifier occurs at a threshold of >0.5 [25]. Consequently, the confusion matrix of the ANFIS model is obtained with a threshold of >0.5 (Table 1).

A performance test for the classifier may involve computation of the sensitivity, specificity and total classification accuracy [25]. The specificity alone provides no information on the degree to which the test recognizes alteration cases; therefore, we also need to calculate the sensitivity of the test. A sensitivity of 100% indicates that the test recognizes all the actual alteration; however,

sensitivity alone does not tell us how well the test predicts other classes. An accuracy of 100% means that the measured values are exactly the same as the target values. The obtained values of the statistical parameters (sensitivity, specificity and total classification accuracy) are given in Table 2. ANFIS classified altered and unaltered pixels in the test data with a sensitivity of 96.75%, specificity of 99.61% and total classification accuracy of 99.10% (Table 2).

5.2.3. Classification of ASTER images for the study area using ANFIS

After training, testing and assessment of the proposed ANFIS model, the entire study area was classified based on the degree of fuzzy membership of the altered class (Figure 8A). The obtained image is scaled between 0 and 1. The ANFIS model can be used with a threshold to produce a binary map. If the ANFIS output is above the threshold, the ANFIS produces a map showing the distribution of alteration; otherwise, a map is produced showing the distribution of unaltered rocks. Figure 8B shows a binary map of ANFIS with a threshold of >0.5.

Table 2. Statistical parameters of the testing and training data.

Statistical Parameters (ANFIS)	Testing Data	Training Data
Sensitivity	96.75%	99.44%
Specificity	99.61%	98.52%
Total classification accuracy	99.10%	98.68%

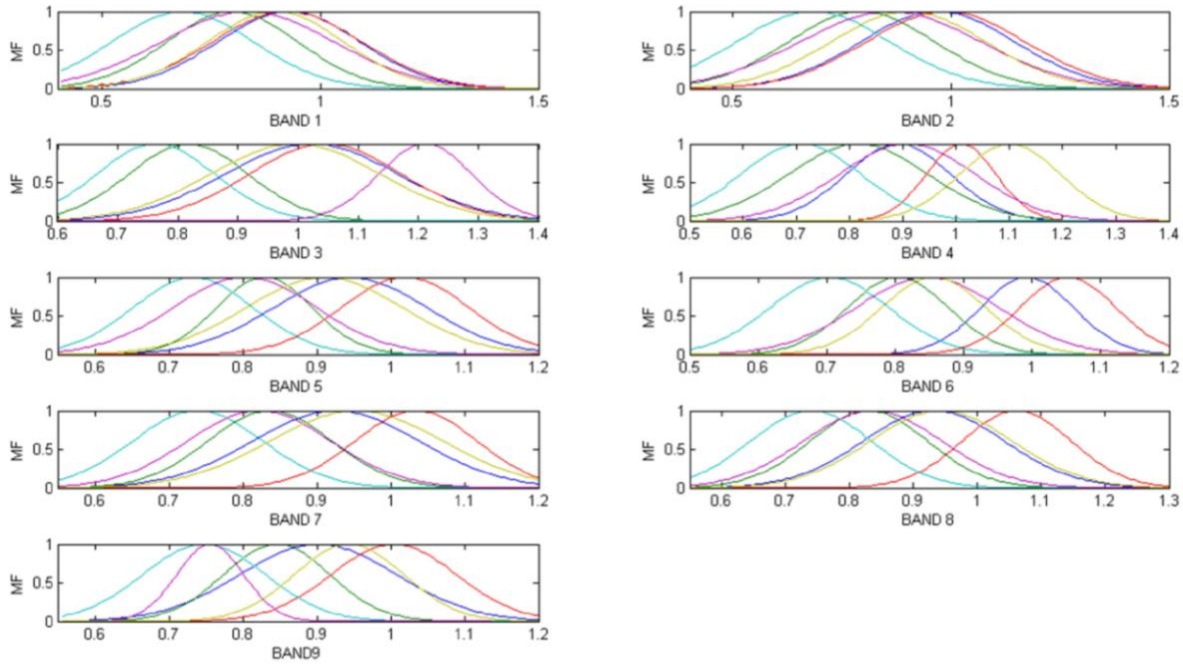

Figure 7. Membership functions obtained by subtractive clustering and further optimization for a model with six rules.

6. Discussion

The main problem encountered in traditional image classification for mapping the distribution of alteration is that, materials unaffected by hydrothermal alteration are erroneously classified as hydrothermal materials, due to the similar spectral properties of the minerals in both altered and unaltered rocks. As discussed above, ASTER data were used for alteration mapping using MLC, ANN and ANFIS. The altered areas, as identified in the classified images, were checked in the field and in the laboratory by observations of thin sections and X-ray diffraction analysis.

Sericite alteration is dominant at the Iju, Serenu, Chahfiroozeh, Meiduk, Parkam, Kader, and Abdar porphyry copper deposits. Two types of phyllic alteration can be identified in the field including ferric-iron-rich and iron-oxide poor phyllic alteration. The iron-oxide-rich phyllic zone contains a large amount of iron oxide minerals on the surface.

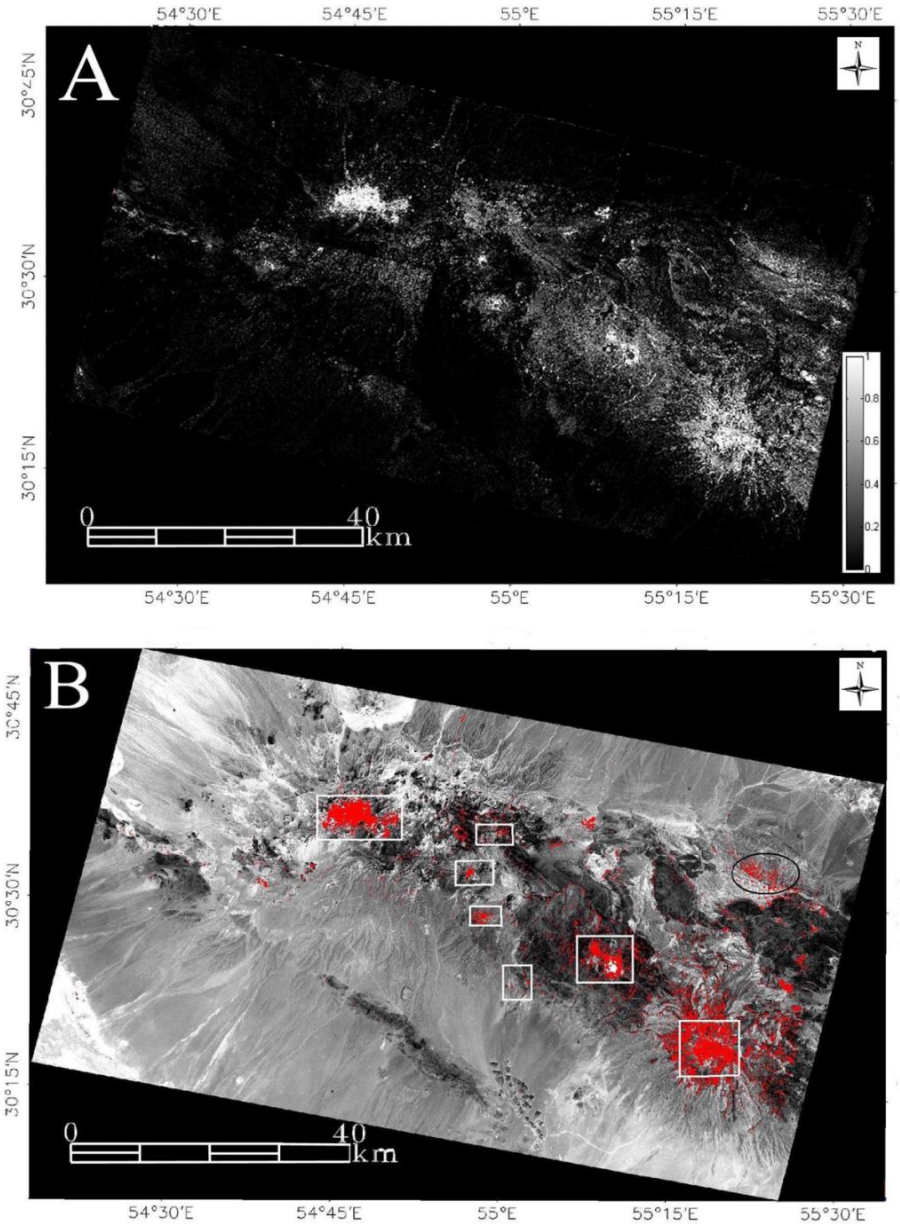

Figure 8. (A) Predicted hydrothermal alteration using the ANFIS (SCM) model. (B) Binary map obtained using the ANFIS model with a threshold of >0.5, draped over band 1 of ASTER. The boxes indicate mineralized areas (see also figure 2).

The iron oxide/hydroxide minerals are in the form of goethite, jarosite and minor hematite which are common secondary minerals at the Kader, Iju, Serenu, Parkam, Meiduk, and Abdar deposits (Figure 9a-g). In the Kader area, three zones of hydrothermal alteration are relatively uniform over an area that includes zones of phyllic, argillic, and propylitic alteration. The feldspars in the altered rocks are converted to kaolinite, illite, and sericite. Because of the difficulties in identification of clay minerals in thin section, we analyzed the rock samples by spectroradiometer. Argillic alteration is present in the deposits at Kader, Serenu, Meiduk, Parkam, Godekolvary and Abdar (Figure 10a).

Because of the presence of minerals such as chlorite and epidote, the spectra of propylitic rocks show strong absorption in 2.33 μm (Figure 10a). Propylitic alteration occurs around most of the mineralized areas. In addition, vein-type mineralization in the area is affected by propylitic alteration. As an example, the Palangi copper deposit is a deposit most strongly dominated by propylitic alteration (Figure 9h). The spectra of iron oxide minerals collected from the area are presented in figure 10b. The detailed characteristics of these deposits are given in Table 3.

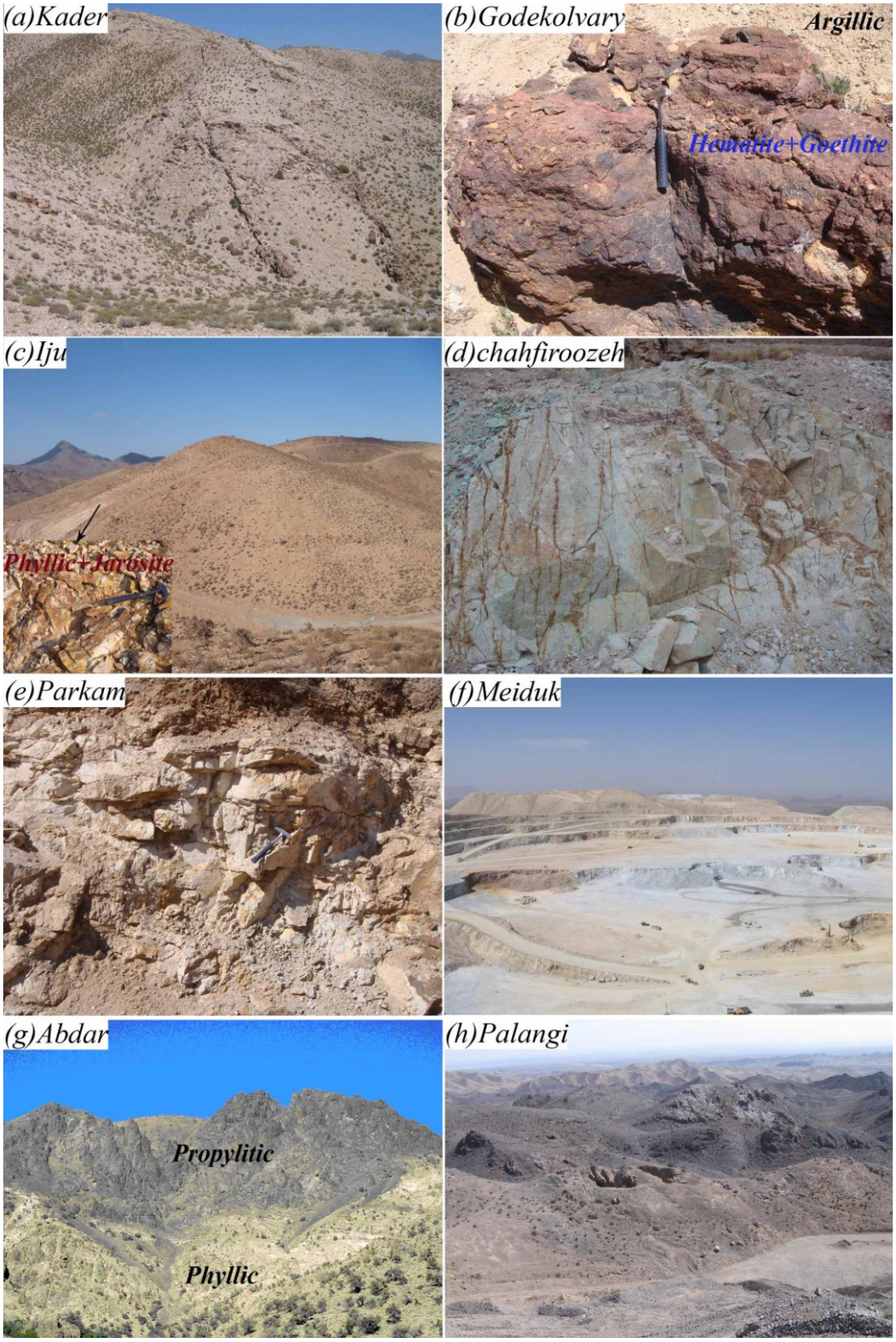

Figure 9. Field photographs of typical alteration zones in the study area. (a) Phyllic alteration zone with silica veinlets, (b) iron oxides (hematite and goethite) with argillic alteration, (c) phyllic alteration and jarositization, (d) phyllic alteration stained with iron oxide and hydroxide minerals, (e) phyllic alteration, (f) regional view of the central alteration zone, (g) phyllic and propylitic alteration zones and (h) regional view of propylitic alteration.

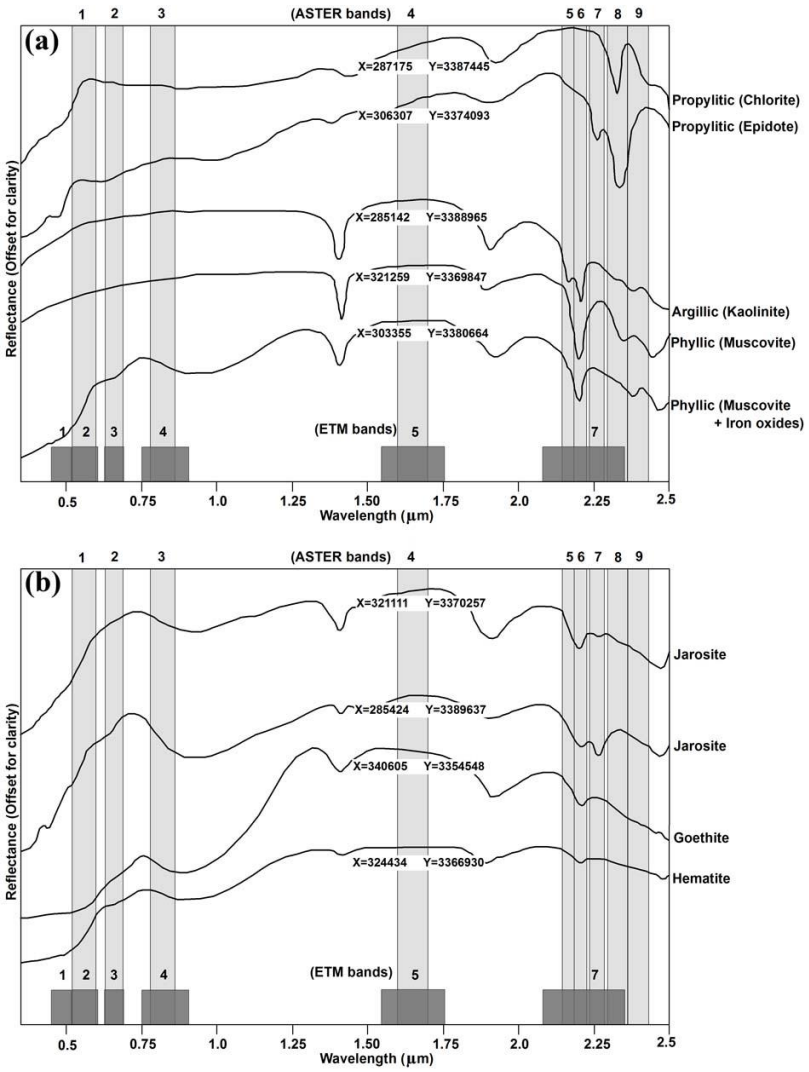

Figure 10. The spectra of the samples from (a) phyllic, argillic and propylitic zones; (b) iron oxide minerals, measured by a field spectroradiometer.The UTM, Zone-40 coordinates of the samples are shown on the spectra.

Figure 7(A) shows the result of ANN classification. A comparison of the altered areas in the image with field data reveals errors in the classified map. Vegetation cover (black circles) and sedimentary rocks (black squares) are enhanced, which are erroneously mapped as areas of alteration. The MLC approach yields similar errors to those produced by the ANN method, and it overestimates the spatial extent of alteration around Abdar (No. 7 in Figure 2) compared with the actual extent on the ground (Figure 7B). These problems are less evident in the classified image obtained by ANFIS (Figure 8B); although an area of sedimentary rock (black ellipse) is erroneously mapped as an area of alteration.

The qualitative assessment of the accuracy of the three methods indicates that ANFIS is a reliable method for alteration mapping, provided that the nature of the training areas is well known. The known distribution of mineralization in the study area is consistent with the distribution of hydrothermal alteration obtained by ANFIS (Figures 2 and 8). Therefore, this technique can be used as an exploration tool in areas with similar climate and geology to those of the present study area.

7. Conclusions

1) A comparison of the results obtained from different classification methods, in terms of the distribution of hydrothermal alteration, showed that the image classified by the ANFIS method yielded the best result.

2) The ANFIS method can be successfully applied in areas that contain similar minerals in altered and non-altered areas, with similar spectral properties, as the method eliminates spectral interference.

3) The known occurrence of mineralization in the study area is consistent with the mapped

distribution of hydrothermal alteration using the ANFIS method.

4) We suggest applying the ANFIS method in exploring for hydrothermal alteration in other parts of the Iranian Cenozoic magmatic belt, which has great potential for copper mineralization.

Acknowledgements

The comments and suggestions by the reviewers of the journal, have greatly improved the quality of the manuscript. Institute of science and high technology and environmental sciences, graduate university of advanced technology provided the spectroradiometer for spectra measurements.

Table 3. Characteristics of the major copper deposits in the study area [26].

	Deposit	UTM coordinates	Type of mineralization	Host rocks	Main alteration types†	Main Altered minerals†	Main ore minerals
1	Kader	X: 285503 Y: 3389840	Porphyry	Diorite porphyry, Quartz diorite porphyry	Phyllic, Argillic, Propylitic, Silicification	Muscovite, Kaolinite, Illite, Quartz, Natroalunite	Pyrite, Chalcopyrite, Chalcocite, Covellite
2	Godekolvary	X: 307128 Y: 3386478	Porphyry	Diorite porphyry, Granodiorite, Andesite	Argillic, Phyllic, Propylitic, Silicification	Kaolinite, Muscovite, Montmorillonite, Quartz, Chlorite, Epidote	Pyrite, Chalcopyrite
3	Iju	X: 303315 Y: 3380542	Porphyry	Diorite porphyry, Quartz diorite porphyry	Phyllic, Argillic, Potassic, Propylitic, Jarositization	Muscovite, Illie, Quartz, Kaolinite, Albite, Chlorite	Pyrite, Chalcopyrite, Chalcocite
4	Serenu	X: 305954 Y: 3374148	Porphyry	Diorite porphyry, Quartz diorite porphyry, Andesite	Phyllic, Argillic, Propylitic, Potassic	Muscovite, Illie, Quartz, Albite, Orthoclase, Kaolinite, chlorite Montmorillonite	Pyrite, Chalcopyrite
5	Chahfiroozeh	X: 309441 Y: 3364244	Porphyry	Granodiorite porphyry	Phyllic, Potassic, Propylitic	Muscovite, Illie, Quartz, Albite, Orthoclase	Malachite, Azurite, Chrysocolla, Pyrite, Chalcopyrite
6	Parkam	X: 321121 Y: 3369859	Porphyry	Diorite porphyry, Micro diorite porphyry	Phyllic, Argillic, Potassic, Propylitic, Jarositization, Silicification	Muscovite, Illie, Quartz, Jarosite, Albite, Orthoclase, Kaolinite	Pyrite, Chalcopyrite, Malachite
7	Meiduk	X: 323885 Y: 3366900	Porphyry	Diorite porphyry	Phyllic, Argillic, Potassic, Propylitic	Muscovite, Illie, Quartz, Jarosite, Albite, Orthoclase, Kaolinite, Montmorillonite	Pyrite, Chalcopyrite, Chalcocite, Malachite
8	Abdar	X: 336271 Y: 3354694	Vein and Porphyry	Granodiorite porphyry, Dasite porphyry, Andesite and diorite	Phyllic, Argillic, Propylitic	Muscovite, Illie, Quartz, Albite, Kaolinite, Montmorillonite, Chlorite	Pyrite, Chalcopyrite, Galena, Malachite
9	Palangi	X: 368910 Y: 3355907	Impregnation	Andesite and pyroclastites	Carbonatization, Propylitic, Chloritization, Sericitization, Silicification	Chlorite, Epidote, Calcite, Quartz	Chalcopyrite, Malachite, Azurite, Chalcocite, Bornite

† Based on field observations, thin section studies, spectral measurements and XRD analysis (This study).

References

[1]. Livo, E., Clark, R.N., and Knepper, D. (1993). SPVIEW Spectral Plot program for accessing the U.S. Geological Survey Digital Spectral Library Database with MS-DOS personal computers: U.S. Geological Survey, Open File Report 93-593, pp 26.

[2]. Yamaguchi, Y., Kahle, A.B., Tsu, H., Kawakami, T., and Pniel, M. (1998). Overview of Advanced Space-borne Thermal Emission and Reflection Radiometer (ASTER). IEEE Transactions on Geosciences and Remote Sensing, 36, 1026–1071.

[3]. Rowan, L.C., Hook, S.J., Abrams, M.J., and Mars, J.C. (2003). Mapping hydrothermally altered rocks at Cuprite, Nevada, using the advanced space-borne thermal emission and reflection radiometer (ASTER), a new satellite-imaging system. Economic Geology 98, 1018-1027.

[4]. Zhang, X., Pazner, M., and Duke, N. (2007). Lithologic and mineral information extraction for gold exploration using ASTER data in the south Chocolate Mountains (California). ISPRS Journal of Photogrammetry and Remote Sensing 62, 271-282.

[5]. Hubbard, B.E., and Crowley, J.K. (2005). Mineral mapping on the Chilean-Bolivian Altiplano using Co-orbital ALI, ASTER and Hyperion imagery: data dimensionality issues and solutions. Remote Sensing of Environment 99, 173-186.

[6]. Mars, J.C., and Rowan, J.C. (2006). Regional mapping of phyllic and argillic altered rocks in the Zagros magmatic arc, Iran, using Advanced Space-borne Thermal and Reflection Radiometer (ASTER) data and logical operator algorithms. Geosphere 2, 161-186.

[7]. Rowan, L.C., Schmidt, R.G., and Mars., J.C. (2006). Distribution of hydrothermally altered rocks in RekoDiq, Pakistan mineralized area based on spectral analysis of ASTER data. Remote Sensing of Environment 104, 74-87.

[8]. Tangestani, M.H., Mazhari, N., Agar, B., and Moore, F. (2008). Evaluating Advanced Spaceborne Thermal Emission and Reflection Radiometer (ASTER) data for alteration zone enhancement in a semi arid area, northern Shahr-e-Babak, SE Iran. International Journal of Remote Sensing 29, 2833-2850.

[9]. Abrams, M.J., Brown, D., Lepley, L., and Sadowski, R. (1983). Remote sensing for porphyry copper deposits in southern Arizona. Economic Geology 78, 591–604.

[10]. Kaufmann, H. (1988). Mineral exploration along the Aqaba–Levant structure by use of TM data; concepts, processing, and results. Int. J. Remote Sensing 9, 1639–1658.

[11]. Knepper, D.H., and Simpson, S.L. (1992). Remote sensing in Geology and mineral resources of the Altiplano and Cordillera Occidental, Bolivia, U.S. Geol. Surv. 47–55.

[12]. Bennett, S.A., Atkinson, W.W., and Kruse, F.A. (1993). Use of thematic mapper imagery to identify mineralization in the Santa Teresa District, Sonora, Mexico. Int. Geol. Rev. 35, 1009–1029.

[13]. Goosens, M.A., and Kroonenberg, S.B. (1994). Spectral discrimination of contact metamorphic zones and its potential for mineral exploration, province of Salamanca, Spain. Remote Sensing of The Environment 47, 331–344.

[14]. Carranza, E.J.M., and Hale, M. (2002). Mineral imaging with LANDSAT thematic mapper data for hydrothermal alteration mapping in heavily vegetated terrane. In: International journal of remote sensing 23, 4827-4852.

[15]. Porwal, A.E., Carranza, J.M., and Hale. M. (2004). A Hybrid Neuro-Fuzzy Model for Mineral Potential Mapping. Mathematical Geology 36, 803-826.

[16]. Honarmand, M., Ranjbar, H., and Shahabpour., J. (2011). Application of Spectral Analysis in Mapping Hydrothermal Alteration of the Northwestern Part of the Kerman Cenozoic Magmatic Arc, Iran, Journal of Sciences 22, 221-238.

[17]. Bodruddoza, M.D., and Fujimitsu., Y. (2012). Mapping hydrothermally altered mineral deposits using Landsat 7 ETM+ image in and around Kuju volcano, Kyushu, Japan, Journal of Earth System Science 121, 1049–1057.

[18]. Jang, J.S.R. (1993). ANFIS: Adaptive-network-based fuzzy inference system. IEEE Transactions on Systems, Man, and Cybernetics. 23, 665–685.

[19]. Lillesand, T., Keifer, R.W., and Chaipman, J.W. (2003) .Remote sensing and image interpretation, Wiley, New York, 763p.

[20]. McCloy, K.R. (2006). Resource management information systems: Remote sensing, GIS and modelling. Taylor and Francis, 575p.

[21]. Akbulut, S., Hasiloglu, A.S., and Pamukcu, S. (2004). Data generation for shear modulus and damping ratio in reinforced sands using adaptive neuro-fuzzy inference system. Soil Dynamics and Earthquake Engineering, 24, 805–814.

[22]. Wang, L.X. (1999). A Course in Fuzzy Systems and Control, Prantice-Hall Inc., 424p.

[23]. Soheili, M. (1981). Geological map of Anar, 1:250 000 map, Geological Survey of Iran publication, Tehran.

[24]. Gokceoglu, C. (2002). A fuzzy triangular chart to predict the uniaxial compressive strength of Ankara agglomerates from their petrographic composition. Engineering Geology, 66, 39–51.

[25]. Fawcett, T. (2004). ROC Graphs: Notes and Practical Considerations for Researchers. Kluwer Academic Publishers, 38p.

[26]. Geological Survey of Iran (GSI). (1973). Exploration for ore deposits in Kerman region. Report No. Yu/53, Tehran, Iran: Ministry of Economy Geological Survey of Iran.